ELSEVIER

Contents lists available at ScienceDirect

Biosensors and Bioelectronics

journal homepage: www.elsevier.com/locate/bios





Strain sensors fabricated by surface assembly of nanoparticles

Han-Wen Cheng a,b,*, Shan Yan b, Guojun Shang b, Shan Wang b, Chuan-Jian Zhong b,**

- ^a School of Chemical and Environmental Engineering, Shanghai Institute of Technology, Shanghai, 201418, China
- ^b Department of Chemistry, State University of New York at Binghamton, Binghamton, NY, 13902, USA

ARTICLE INFO

Keywords: Surface assembly Metal nanoparticles Strain sensors Interparticle spatial properties Intermolecular interactions Wearable sensors

ABSTRACT

Harnessing interparticle spatial properties of surface assembly of nanoparticles (SAN) on flexible substrates is a rapidly emerging front of research in the design and fabrication of highly-sensitive strain sensors. It has recently shown promising potentials for applications in wearable sensors and skin electronics. SANs feature 3D structural tunability of the interparticle spatial properties at both molecular and nanoscale levels, which is transformative for the design of intriguing strain sensors. This review will present a comprehensive overview of the recent research development in exploring SAN-structured strain sensors for wearable applications. It starts from the basic principle governing the strain sensing characteristics of SANs on flexible substrates in terms of thermallyactivated interparticle electron tunneling and conductive percolation. This discussion is followed by descriptions of the fabrication of the sensors and the proof-of-concept demonstrations of the strain sensing characteristics. The nanoparticles in the SANs are controllable in terms of size, shape, and composition, whereas the interparticle molecules enable the tunability of the electrical properties in terms of interparticle spatial properties. The design of SAN-derived strain sensors is further highlighted by describing several recent examples in the explorations of their applications in wearable biosensor and bioelectronics, Fundamental understanding of the role of interparticle spatial properties within SANs at both molecular and device levels is the focal point. The future direction of the SAN-derived wearable sensors will also be discussed, shining lights on a potential paradigm shift in materials design in exploring the emerging opportunities in wearable sensors and skin electronics.

1. Introduction

Wearable and stretchable strain sensors have become one of the fastest growing cutting-edge fields for human-machine interfacing and personalized healthcare-performance monitoring. Materials such as polymers, fibers, graphenes, carbon nanotubes, etc. are widely explored for the design and fabrication of strain sensors (Seyedin et al., 2019; Souri et al., 2020), with sensing mechanisms ranging from resistive changes in structural connecting/disconnecting, microcrack opening/closing and current tunneling, to capacitive or optical changes in materials geometric dimension (Ho et al., 2017; Seyedin et al., 2019; Souri et al., 2020; You et al., 2016). The development of polymer nanocomposite-based wearable strain sensors for bio-monitoring (Lu et al., 2019) has brought quite some interest in the field of wearable sensors (Someya et al., 2016; Wei et al., 2016; Wu et al., 2016; Yang et al., 2016; Zhang et al., 2017a). There has been a surge of interest in the fabrication of wearable sensors, which constitutes one of the frontiers of research in personalized health monitoring technologies (Bae et al., 2018; Chun et al., 2019; Dinh et al., 2020; Gao et al., 2017; Hua et al., 2018; Khoshmanesh et al., 2021; Li et al., 2016b; Park et al., 2017; Wang et al., 2016; Zhou et al., 2020a). There has been an extensive coverage of these strain sensors in terms of performance parameters, such as sensitivity, linearity, stretchability, durability, and hysteresis (Seyedin et al., 2019; Souri et al., 2020). Some of the major approaches to fabricating wearable and stretchable strain sensors have focused on the use of polymers and carbon materials as sensing materials, demonpromising applications healthcare-performance monitoring (Chen et al., 2021; Meng et al., 2020; Yang et al., 2015; Zhang et al., 2017b, 2021; Zhou et al., 2020b). These sensors feature tunable stretchability and self-powering function, which constitute major advantages in wearable applications. In comparison with the significant progress and enormous interests in the development of the wearable sensors based on the approaches of polymers and carbon materials to the fabrication, relatively limited attention is paid to the strain sensors derived from the approach from surface assembly of nanoparticle (SAN). While the study of SAN-derived strain

^{*} Corresponding author. School of Chemical and Environmental Engineering, Shanghai Institute of Technology, Shanghai, 201418, China.

^{**} Corresponding author. Department of Chemistry, State University of New York at Binghamton, Binghamton, New York, 13902, USA. *E-mail addresses*: hwcheng@sit.edu.cn (H.-W. Cheng), cjzhong@binghamton.edu (C.-J. Zhong).

sensors has not reached the level of extensive applications as polymer or carbon materials derived sensors, it is a rapidly emerging front of active research in design and fabrication of highly-sensitive strain sensors. This review will present a comprehensive overview of the recent development of research in SAN-structured strain sensors for wearable applications.

SANs feature intermolecular interactions dictated by interparticle spatial properties in a 3D architecture, exhibiting a strong dependence on particle size in the range of 10-20 nm (Cometto et al., 2017). Nanoparticles (NPs) of metals such as gold (Au) and silver (Ag) feature size- and shape-dependent radius of curvature in comparison with traditional flat metals. With the expansion of Au(I)-thiolate chemistry to gold nanoclusters (NCs) and NPs (Jin et al., 2016), there has been a paradigm shift in the design of functional surfaces or interfaces using NCs and NPs as the building blocks. The assembly of NCs or NPs on a substrate surface creates an intriguing class of SANs for the fabrication of strain sensors with molecularly-tunable sensitivity of the interparticle spatial properties, which have found a wide range of applications for wearable sensors and skin electronics. The interparticle spatial properties of SANs are tunable not only by the intrinsic interparticle distance, particle size, and shape, but also by the curvature of the substrate. The interparticle molecular structures can range from small to larger inorganic/organic molecules as well as biomolecules such as DNAs and proteins with intermolecular interactions range from covalent, ionic, hydrogen bonding and van der Waals forces. On a flexible substrate, the interparticle distance depends on strains of the substrate, producing "squeezed" interparticle molecular interdigitation upon compressive strain or "loosened" interparticle molecular interdigitation upon tensile strain. Such molecularly-tunable strain/gauge or chemical/bio sensors present enormous opportunities in wearable sensors and skin electronics (Broza et al., 2018; Kahn et al., 2015; Ketelsen et al., 2018; Lee et al., 2017a, 2017b, 2018; Liao et al., 2017; Niu et al., 2019; Oh and Bao, 2019; Segev-Bar et al., 2015a; Vishinkin and Haick, 2015; Yi et al., 2016). The control of the interparticle spatial properties is essential in exploring the functional properties of SANs for the design of strain sensors on flexible substrates (Kang et al., 2016; Shan et al., 2014; Yin et al., 2011; Zhao et al., 2015a, 2015b). For SANs derived from Au-based NCs or NPs, it takes advantage of the well-defined molecular tunability of Au(I)-thiolate chemistry and the molecular functional properties (Casanova-Cháfer et al., 2019; Colangelo et al., 2017). The assembly on atomically-flat or nanoscale-curved surfaces (Kong et al., 2016, 2018; Song et al., 2016) also serves as a model system for designing molecular electronics (Casalini et al., 2017; Seo et al., 2017; Xiang et al., 2016) for various applications (Baghbanzadeh et al., 2017; Chen et al., 2017; Jiang et al., 2015b; Newcomb et al., 2014; Thompson and Nijhuis, 2016; Yuan et al., 2018). By highlighting the recent development in exploring SANs for design and fabrication of strains sensors, this article serves as a springboard to understanding of the role of interparticle spatial properties and intermolecular interactions at both molecular and device levels. In this review, the SAN-derived strain sensors will be discussed, focusing on three related topic areas, including the general characteristics of SAN in terms of the nanoparticle assembly, the sensing interface, and the strain sensor application perspectives (Fig. 1).

The ability to harness the interparticle spatial properties constitutes a key factor in the design of SAN-derived strain sensors. The recent progress has indeed presented increasing opportunities for their applications in biosensors and bioelectronics, especially in the fields of personal healthcare and human machine interfacing. Mechanistically, the understanding of the interparticle spatial properties and the resulting resistive or capacitive mechanisms in SANs is essential in converting the strain changes into electrical signals. This understanding, while still at its early stage in comparison with the widespread applications of conventional polymer and carbon materials-based strain sensors and the emerging explorations of triboelectric nanogenerators or piezoelectric nanogenerators for strain sensors (Chen and Wang, 2017; Tat et al., 2021; Zhou et al., 2020c), is presenting intriguing opportunities for the

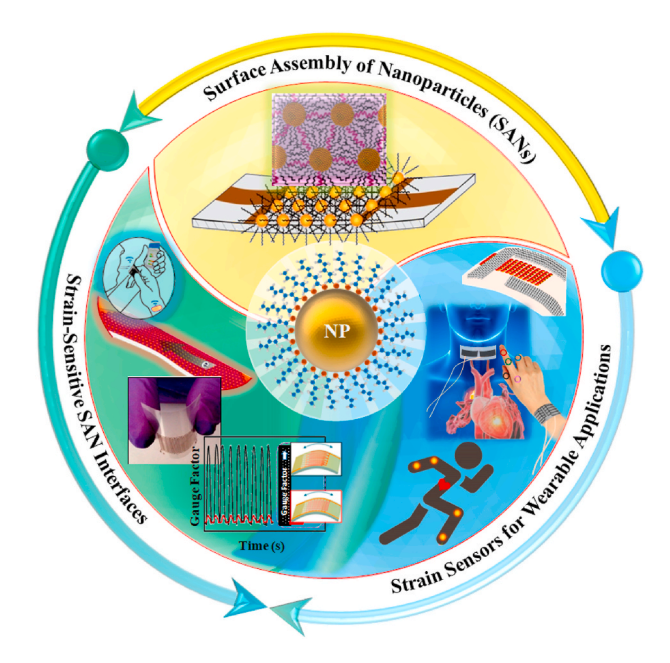


Fig. 1. Illustration of SANs in terms of the nanoparticle (NP) assembly, the sensing interface, and the strain sensor application.

research community in developing wearable sensors. Selected examples will be highlighted in this review.

2. Basic characteristics of SAN-Derived strain sensors

Thermally-activated conduction theory. In a typical SAN, a key element dictating the interfacial sensing characteristics is the interparticle molecular interactions, which plays a major role in the nanoparticle-ligand ensemble or collective properties, such as electrical and optical properties. In contrast to exploiting changes in structural connecting/disconnecting, microcrack opening/closing, current tunneling and materials geometric dimension (Ho et al., 2017; Seyedin et al., 2019; Souri et al., 2020; You et al., 2016), harnessing the interparticle spatial properties is an intriguing pathway for the design of strain sensors. Perturbation of the intermolecular interactions can be induced by device strains, leading to a change in electrical properties of the SAN. The exponential dependence of the interparticle electron tunneling conductivity on the particle separation in assemblies of gold NPs was exploited (Herrmann et al., 2007; Sangeetha et al., 2013) as the basis of sensitive strain sensors, with the gauge factor depending on the NP radius (r) and interparticle distance (δ). The overall electrical conductivity (σ) is related to the activation energy in a thermally–activated conduction path (Yin et al., 2011):

$$\sigma(\delta, T) = \sigma_0 \exp(-\beta \delta) \exp(\frac{e^2}{8\pi\varepsilon\varepsilon_0 RT} (\frac{1}{r+\delta} - \frac{1}{r}))$$
 (1)

where $e=1.6\times 10^{-19}$ C, $\varepsilon_0=8.854\times 10^{-12}$ F/m, $R=1.38\times 10^{-23}$ J/K, σ_0 is a pre-factor, T is temperature, ε is dielectric medium constant, and β is electron coupling constant. The activation energy (Ea) for activated electron tunneling depends on r, δ and ε . The detailed tunability of the electrical conductivity in terms of β , r, δ and ε has been validated by experimental results for SANs derived gold nanoparticles of different sizes and molecular linkers of difference spacing (Wang et al., 2007a, 2007b). For example, the electrical conductivity of a thin film assembly of alkanethiolate-capped gold nanoparticles of 2 or 4 nm diameters linked by alkyl dithiols of different chain lengths (0.8–2 nm) on interdigitated microelectrodes showed not only size dependence but also the alkyl thiol chain length dependence (Wang et al., 2007a). This finding demonstrated a clear linear relationship between the logarithm of

electrical conductivity ($Ln\sigma$) and the interparticle spacing (δ), revealing a β value of 0.4–0.7 A⁻¹ for SANs with Au nanoparticles of 2 and 4 nm diameters, respectively.

Interparticle spatial properties. Broadly speaking, SAN consists of nanoscale and molecular scale building blocks, which can be defined as nanoscale "bricks" glued by molecular "spacers". In the case of using nanoparticles as the "bricks" and molecules/biomolecules as the "spacers", Fig. 2 illustrates the general concept, which highlights the two major factors influencing the performance of SANs as strain sensors, as will be discussed in later sections, in terms of nanoparticle parameters (size, composition, and shape, etc.) and ligand chemistry (e.g., linking/capping molecules). For the ligand chemistry, one of the most popular approaches stems from the early well-defined surface chemistry of organothiols on planar coinage metal substrates such as gold, silver and copper (Cheng et al., 2019, 2021; Love et al., 2005), and advances to the molecular capping/linking chemistry on the nanoparticle counterparts of the coinage metals (Hostetler et al., 1998), which constitutes the basic building blocks of SANs.

For SAN, the combination of the ligand chemistry and nanoparticle parameters defines the interparticle spacing and electrical properties in an ensemble of nanoparticles. Indeed, for SANs with gold nanoparticles of different sizes and alkyl linking molecules of different chain lengths, both the logarithm of conductivity (σ) and the activation energy (E_a) scale linearly or approximately linearly with the number of methylene groups (n) in the alkyl chain or the length of the alkyl chain (Fig. 2B), which are consistent with the thermally-activated conductivity theory (Eq. (1)) (Wang et al., 2007a). For a change in the interparticle distance $(\Delta \delta = \delta_2 - \delta_1)$, there is a corresponding change in σ , $\Delta \sigma = \sigma_2 - \sigma_1$, or in resistance (R_1 to R_2), i.e., $\Delta R/R_1$ ratio, which can be derived from Eq. (1) $(\sigma \propto 1/R)$ (Yin et al., 2011). For SAN on a flexible substrate (Length L, and thickness T_s), bending of the substrate causes a change in device strain, the degree of which depends on the radius of curvature (R_b). With a device bending from flat (d_1) to bent (d_2) , i.e., $\Delta L (= d_2 - d_1)$, which is directly linked to δ_i and $\Delta \delta$, respectively, the device strain ($\varepsilon_{\text{strain}}$) can be expressed by the ratio of $\Delta L/L$. The device strain ($\varepsilon_{\text{strain}}$) is expressed as:

$$\varepsilon_{Strain} = \frac{\Delta L}{L} = \frac{d_2 - d_1}{2r + d_1} = \frac{T_s}{2R_b}$$
 (2)

where d_i and ΔL for SAN on flexible substrate correspond to δ_i and $\Delta \delta_i$ respectively, as defined for the interparticle distance and its change. Substituting Eq. (2) into Eq. (1), $\Delta R/R_1$ ratio can be derived as a function of strain $\varepsilon_{\text{strain}}$ and R_{b} (Yin et al., 2011; Zhao et al., 2015a). As shown in Fig. 3A for both tensile strain and compressive strain, $\Delta R/R_1$ increases with $\varepsilon_{\mathrm{strain}}$, the magnitude of which is larger for tensile strain than that for compressive strain (Fig. 3B). The magnitude of $\Delta R/R_1$ also depends on particle size and β value. As a strain sensor, the gauge factor, g, is a scale of the sensitivity of strain gauge (Shan et al., 2014) (g = $(\Delta R/R_{\rm flat})/\varepsilon_{\rm strain} = (\Delta R/R_{\rm flat})/(\Delta L/L)$, which depends on $\varepsilon_{\rm strain}$ for both tensile and compressive strains. For SAN films with subtle differences in the linking molecules (e.g., 1,9-nonadithiol (NDT) vs. 11-mercaptoundecanoic acid (MUA)), the magnitude of $\Delta R/R_1$, or the g-factor, strongly depends on the combination of the bending and geometric effects in a significant way. In addition, $\Delta R/R_1$ also responses to chemical perturbation of the interparticle spatial properties, e.g., upon adsorption of organic vapor molecules. This perturbation induces changes in interparticle distance, $\Delta\delta$, and dielectric medium permittivity in the SAN, leading to a change in the electrical resistance (Olichwer et al., 2016), which can also be derived from Eq. (1).

Harnessing the interparticle spatial properties of SAN-derived strain sensors (Segev-Bar et al., 2015a; Zhao et al., 2015b) differs from exploring the intrinsic properties of nanowires in nanowire-based mechanical sensors (Li et al., 2016a; Wu et al., 2013) due to tunability of the intermolecular interactions in the nanostructure of SAN (Fig. 3A). Examples include, e.g., difunctional or multifunctional molecules ranging from simple alkylthiols to complex dendrimers, DNAs or proteins for assembling Au NPs as sensing interfaces for chemical or gauge sensors (Zhao et al., 2015a). In addition to exchange-crosslinking precipitation and stamping patterning methods, there are many different methods for the assembly (Jiang et al., 2015a; Ketelsen et al., 2018; Lee et al., 2017b; Yi et al., 2015), including layer-by-layer self-assembly,

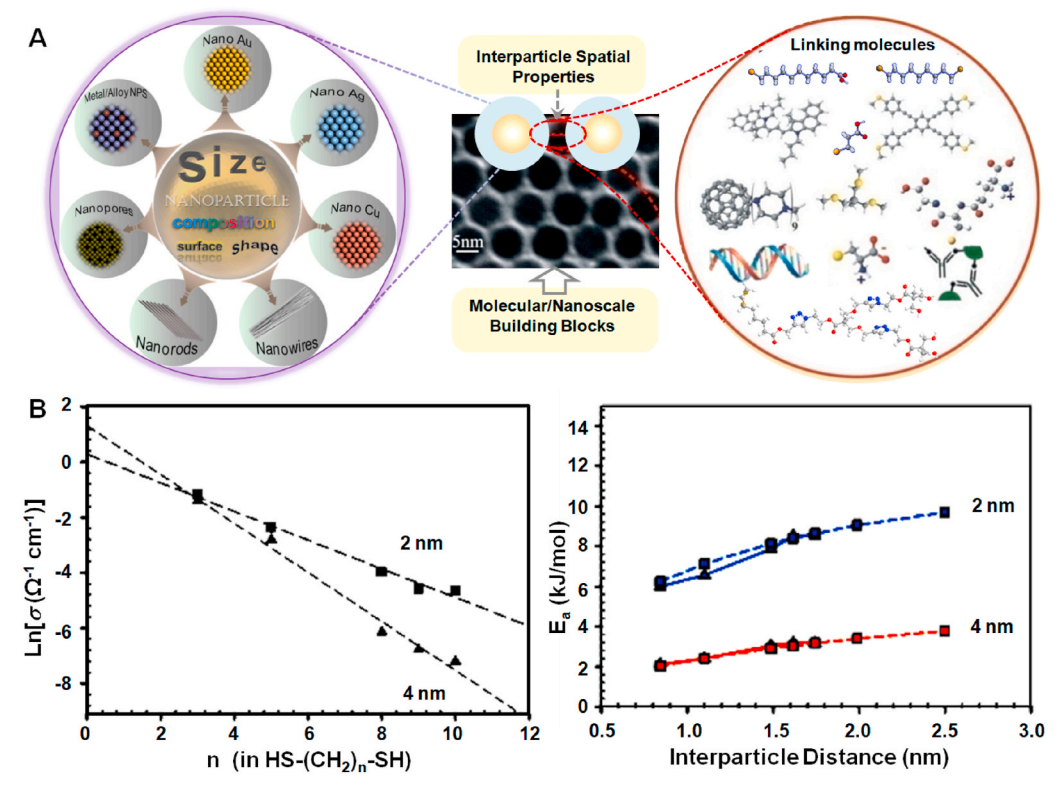


Fig. 2. Illustration of SANs in terms of interparticle spatial properties. (A) Illustration of SAN consisting of nanoscale particles and molecular/biomolecular spacers as the building blocks. (B) Left: Plot of Ln (σ) as a function of the number of methylene groups (n) in the alkyl chain for thin film assemblies of gold nanoparticles of 2.0 nm (filled squares) and 4.0 nm (filled triangles) diameters; Right: Plot of activation energy (Ea) as a function of interparticle distance in the two assemblies, comparing experimental (solid lines, triangle) and calculated results (dashed square). Reproduced with permission (Wang et al., 2007a) Copyright 2007 Royal Society of Chemistry. (For interpretation of the references to colour in this figure legend, the reader is referred to the Web version of this article.)

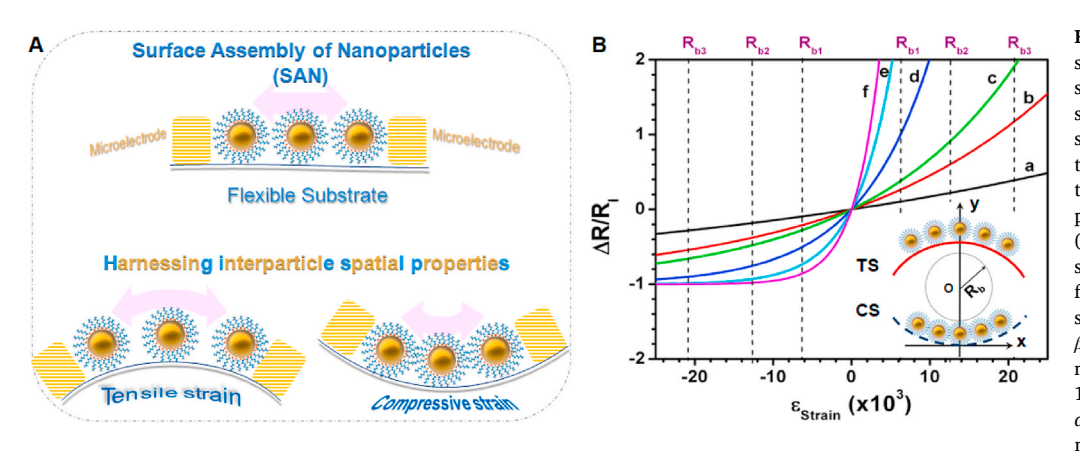


Fig. 3. Basic principle of SAN-derived strain sensors: (A) Illustrations of strain sensing in terms of interparticle spatial properties for SAN on a flexible substrate, where the rectangles illustrate microelectrodes (e.g., interdigitated gold microelectrodes) printed on a polymer (polyethylene terephthalate (PET), polyimide (PI), etc.) or paper substrate. (B) $\Delta R/R_1$ vs. $\varepsilon_{\text{strain}}$ ($\varepsilon=10$), for tensile strain (TS) and compressive strain (CS): (a) r = 1.0 nm, $d_1 = 1.6$ nm, $\beta = 4.0 \text{ nm}^{-1}$, (b) r = 1.0 nm, $d_1 = 1.6$ nm, $\beta = 10 \text{ nm}^{-1}$, (c) r = 4.0 nm, $d_1 =$ 1.0 nm, $\beta = 10 \text{ nm}^{-1}$, (d) r = 10.0 nm, $d_1 = 1.0 \text{ nm}, \beta = 10 \text{ nm}^{-1}, \text{ (e) } r = 20.0$ nm, $d_1 = 1.0$ nm, $\beta = 10$ nm⁻¹, (f) r =30.0 nm, $d_1 = 1.0$ nm, $\beta = 10$ nm⁻¹. Inset: illustration of CS and TS in terms

of radius of curvature (R_b). Reproduced with permission (Yin et al., 2011) Copyright 2011 American Chemical Society. (For interpretation of the references to colour in this figure legend, the reader is referred to the Web version of this article.)

multistep photolithographic patterning, contact printing, etc. The electrical conductivity of the assembly (Jiang et al., 2015a; Lee et al., 2017b; Liao et al., 2017; Yi et al., 2016) exhibits high sensitivity to strains depending on particle size (Segev-Bar et al., 2015b), interparticle distance (Yi et al., 2016), ligands or linker structures, especially the radius of curvature (R_b) in the case of flexible substrates. For example, a discontinuous metal NP film (Yi et al., 2016) could exhibit a strain gauge characteristic with a response frequency in 1-10 Hz range. For an Au NP film on a paper substrate (Liao et al., 2017), the microcrack-based resistive bending strain responses could exhibit a rapid relaxation time of 20 ms and a high stability up to 1.8×10^4 cycles. Disordered interparticle tunneling is also shown to introduce microscopic detour of charge conduction depending on the direction of strain, exhibiting high stability of 7×10^4 bending cycles (Jiang et al., 2015a). With patches featuring antiparallel thickness gradients of NPs (Segev-Bar et al., 2015a), the formation of cracks during NP sintering could lead to a g-factor as high as 300. Moreover, by constructing a sandwich-like stacked graphene and Ag-nanowires hybrid structures, the transparent, bendable, and stretchable strain sensors exhibit a stretchability up to 200%, and transparency of 85% (Li et al., 2016a), with a response time of <1 ms. By assembling a monolayer of Au NPs (Yi et al., 2015), ultrafast dynamic strain response to acoustic vibration without detectable hysteresis is also demonstrated, showing a detection range of 1–20, 000 Hz and a detection limit as low as 0.03%.

Anisotropic gauge properties. One way to understand the g-factor, especially anisotropic gauge properties (Zhao et al., 2015a), in terms of interparticle spatial properties involves analysis of conductive (metal particles) and insulative (interparticle capping/linking molecules) components. The resistivity (ρ) thus depends on the volume fraction change in the form of $\rho = \rho^0 (v_{\rm m} - v_{\rm c})^{-t} (v_{\rm m}$: volume fraction of the metal particles, v_c : critical volume fraction of the conductive phase at the percolation threshold; ρ^0 : a pre-factor), where the value of the critical exponent (t) is closely linked to the dimensionality of SAN. A theoretical-experimental agreement has been demonstrated in terms of the increase of electrical resistance (R) with a decrease of $v_{\rm m}$ (Fig. 4). For SAN of Au NPs with MUA as interparticle linkage, the resulting v_c value (0.124) translates to an interparticle spacing of 1.6 nm for 2-nm Au NPs, which is quite close to the expectation for the SAN with MUA-linked Au NPs. By further translating the relationship between electrical R with $\nu_{\rm m}$ to the relationship between the g-factor and $v_{\rm m}$ for a typical strain (Fig. 4 (inset)), the g-factor displays a sharp increase in the vicinity of v_c . An anisotropic character for the g-factors between B₁ (device bending in perpendicular to current flow (I)) and B_{//} (device bending in parallel to I) is thus expected. This character derives from the differences of the change in the electrical resistance and the volume fraction as a result of

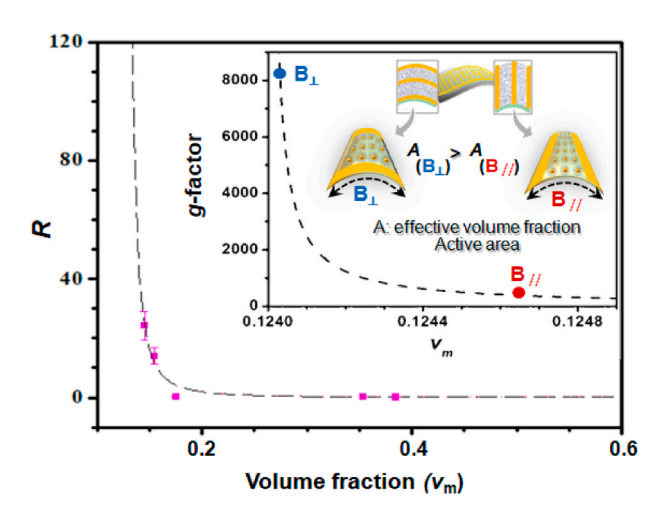


Fig. 4. Plot of the electrical resistance (R, $M\Omega$) vs. volume fraction (ν_m) in the SAN with Au NPs. Dotted line: curve fitting based on percolation theory, inset: theoretical plot of gauge factor (g) vs. ν_m at near percolation threshold ν_c , (red dot: g=383 (B $_{//}$: $\nu_m=0.12465$); blue dot: g=8253 (B $_{\perp}$: $\nu_m=0.12403$)), the calculated g values for B $_{//}$ and B $_{\perp}$ orientations based on the model shown in inset. Reproduced with permission (Zhao et al., 2015a) Copyright 2015 Wiley-VCH. (For interpretation of the references to colour in this figure legend, the reader is referred to the Web version of this article.)

the subtle change in the relative active area near the percolation threshold (Fig. 4 (inset)). Since the change in volume fraction depends on the active surface area in the microelectrode-defined spaces, the corresponding change in resistivity can be expressed in terms of the derivatives of resistivity ($d\rho$) and volume fraction ($dv_{\rm m}$) (Zhao et al., 2015a), i.e., $d\rho/\rho = -t \times dv_{\rm m}/(v_{\rm m} - v_{\rm c})$. Under tensile strain-bending, there is an increase of the gap in the case of B//, and an increase in the microelectrode finger length in the case of B₁ near the percolation threshold ($v_c = 0.124$), the latter of which produced a larger increase in active area than the former (Zhao et al., 2015b). This subtle difference in the active surface area leads to a subtle difference in the change of volume fraction, and its occurrence near the percolation produces a large difference in g-factor (Fig. 4 (inset)). In other words, B_{//} features a change in the gap area with limited dependence on the film thickness, displaying a small decrease of v_m/v_c , whereas there is a relatively larger change in the active area for B_{\perp} as reflected by the length increase in microelectrode fingers (Zhao et al., 2015a).

3D site percolation model. The conductive percolation in terms of

the nanoscale structure - strain sensitivity correlation is further highlighted by 3D site percolation models. The gauge properties of the shellbinary NP self-assembly (Fig. 5A) are modeled as a function of the volume fraction ratio (Zhang et al., 2018), revealing several orders of magnitude changes for the electrical conductivity and the g-factor. Effective medium theory (EMT) using 3D site percolation model is used to simulate the electrical and electro-mechanical properties in terms of packing patterns. Au nanoparticle cores with different shells are mixed to form binary mixtures at defined mixing ratios (different volume fractions) and assembled as two types of shell-binary NP materials (SBNMs), homogeneous ho-SBNMs and heterogeneous he-SBNMs. Percolation driven metal-insulator transition is studied using EMT in terms of the correlation of the electron transport regimes and microscopic arrangements of NPs with the macroscopic properties of the SBNMs. Citrate-stabilized Au NPs (CIT-AuNPs), bisphenylphosphine dihydrate dipotassium salt-stabilized Au NPs (BSPP-AuNPs), and 11-mercaptoundecanoic acid-modified Au NPs (MUA-AuNPs) (~18 nm) are used to form SBNMs. Different conductivities and g-factor are observed as a function of the volume fraction (e.g., ho-SBNMs (BSPP-AuNP/MUA-AuNP) (Fig. 5B) and he-SBNMs AuNP/BSPP-AuNP) (Fig. 5C)). The conductivity threshold in terms of volume fraction is simulated using the approximate dimension ratio of the ho-SBNM stripes, revealing a shift of the threshold to higher values with the increased length or a decreased cross-section (Fig. 5D). The simulation result revealed a threshold of ~37% for ho-SBNM (Fig. 5D) and ~48% for he-SBNM. The electron tunneling path is operative between the BSPP-AuNPs and MUA-AuNPs in ho-SBNMs, differing subtly from that in he-SBNMs. This finding demonstrates a strong correlation between the charge transport and arrangements of NPs in SBNMs to impact the electro-mechanical strain sensing properties (Zhang et al.,

2018; Zhao et al., 2015a), which serves as a guiding principle in the design of strain or gauge sensors with high sensitivity (Lee et al., 2017b).

3. Sensing characteristics to tensile/compressive strains and strain orientation

Sensor Fabrication. A SAN-based strain sensor consists two important elements: the sensitive SANs and the electrical signal transduction electrodes. For the sensitive SANs, the ability to control the nanoparticle morphologies and the ligand structures are essential for achieving the desired sensing sensitivity. There are many pathways to the fabrication of SANs, including casting, layer-by-layer assembly, molecularly-mediated self-assembly, stamping, and printing (Lim and Zhong, 2009; Wang et al., 2010). Some of the earlier pathways start from the synthesis of molecularly-capped metal nanoparticles, including mostly the coinage metals (Au, Ag, Cu, and their nanoalloys). For the molecularly-capped nanoparticles and the molecularly-mediated self-assembly, the surface and interfacial chemistry such as ligand exchange reaction and ligand cross-interaction between nanoparticles, capping molecules and mediator molecules dictates the processes for the interparticle linkages and the assembly of the nanoparticles on the substrate. Fig. 6 illustrates some examples to highlight the abilities to control the surface/interface chemistry with alkanethiols, functionalized alkyl thiols, and gold nanoparticles to define the interparticle spatial properties collectively in ensembles or thin films. The ensembles or thin films can be formed on flexible substrates, such as PET, PI, papers, and other materials, printed with interdigitated microelectrodes, which can then be exploited for the targeted chemical, biological, and strain sensing applications. Due to the molecular capping and interparticle linking structures in the continuous thin film, a relatively-high stability for some

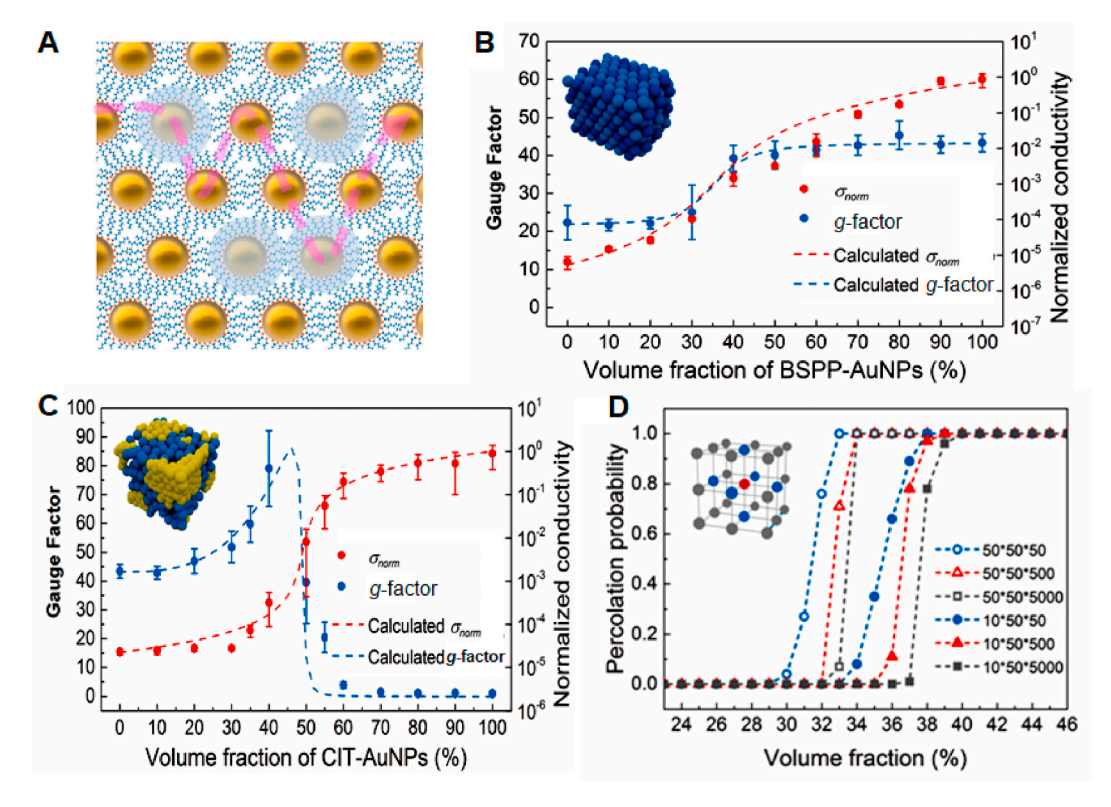


Fig. 5. Theoretical simulation of the strain sensors. (A) Illustration of the electron tunneling path in a SAN with binary nanoparticles in terms of percolation theory. (B-C) Plots of the normalized conductivity (σ_{norm} (red dots)) and g-factor (blue dots) as a function of the volume fraction for two model systems: (B) ho-SBNMs (BSPP-AuNP/MUA-AuNP) and (C) he-SBNMs (CIT-AuNP/BSPP-AuNP), as shown in the insets. (D) Plots of the simulated percolation probability as a function of volume fraction based on cubic lattice model (inset), revealing the percolation threshold for different strip dimensions (height \times width \times length; numbers refer to the number of particles). The slopes become steeper with the numbers of the spheres, the abscissa of which indicates the percolation threshold. Reproduced with permission (Zhang et al., 2018) Copyright 2018 Royal Society of Chemistry. (For interpretation of the references to colour in this figure legend, the reader is referred to the Web version of this article.)

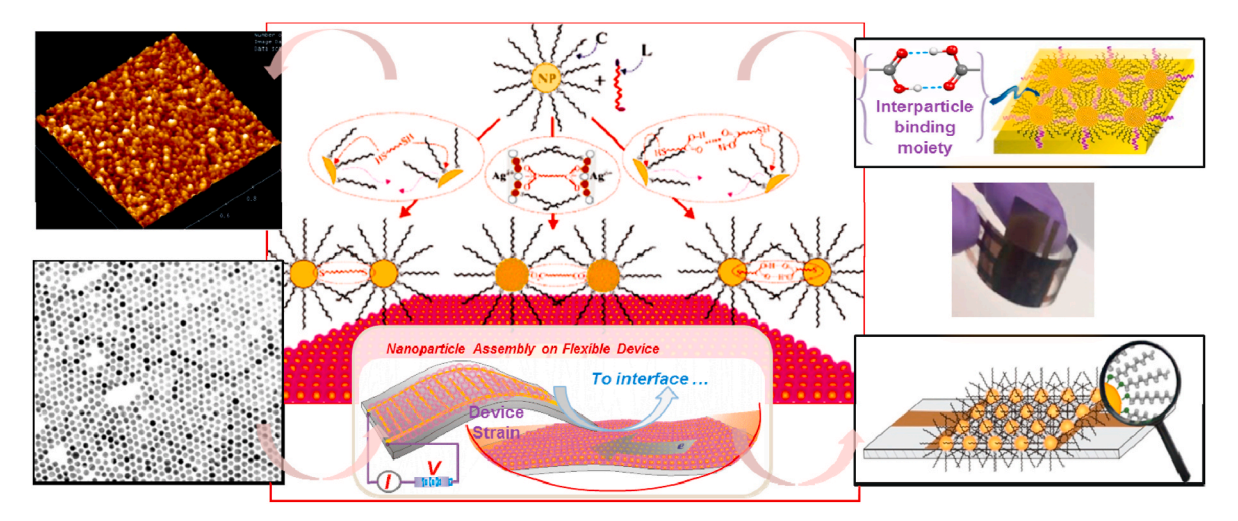


Fig. 6. Illustration of the fabrication of SANs derived from Au NPs on flexible substrates printed with microelectrodes via surface/interfacial linkages or interactions of alkanethiols and functionalized alkyl thiols to define the interparticle spatial properties collectively in ensembles or thin films.

of the SANs under the targeted sensing conditions has been observed (Shan et al., 2014; Zhao et al., 2015b), demonstrating the important role of molecular capping and linking in the overall interparticle structures and properties.

For the electrical signal transduction electrode, the traditional fabrication pathway is photolithographic patterning which is limited by the high cost, the materials limitation, and the manufacture scalability. In addressing these limitations, printing conductive inks with low-temperature and roll-to-roll processing conditions has become an increasingly attractive pathway for the fabrication with flexible substrates. Two recent approaches (Yan et al., 2020; Zhao et al., 2015b) to exploring AuCu alloy NPs as the building blocks for fabricating SANs further highlight this point. One example involves pulsed laser sintering

of NPs on flexible substrates (Zhao et al., 2015b). As illustrated in Fig. 7A, pulsed-laser sintering provides an effective way to convert printed $\text{Cu}_n\text{Au}_{100\text{-}n}$ NPs with controllable size and composition to a conductive pattern or footprint on a flexible substrate with a controllable thermal penetration. The nanoalloy features an enhanced air stability in comparison with pure Cu NPs and decreased melting point in comparison with bulk alloy counterparts due to nanoscale alloying. A focused pulsed laser beam is scanned over the nanoink-printed substrate under a specific speed and power, and the unsintered ink is subsequently dissolved (Fig. 7B). Line widths of 80–400 μ m are easily generated for the sintered NPs. The dependence of sintering on laser wavelength reflects the effective surface plasmonic resonance. Use of a 355-nm pulsed laser was shown to be effective for sintering both Au and CuAu alloy NPs

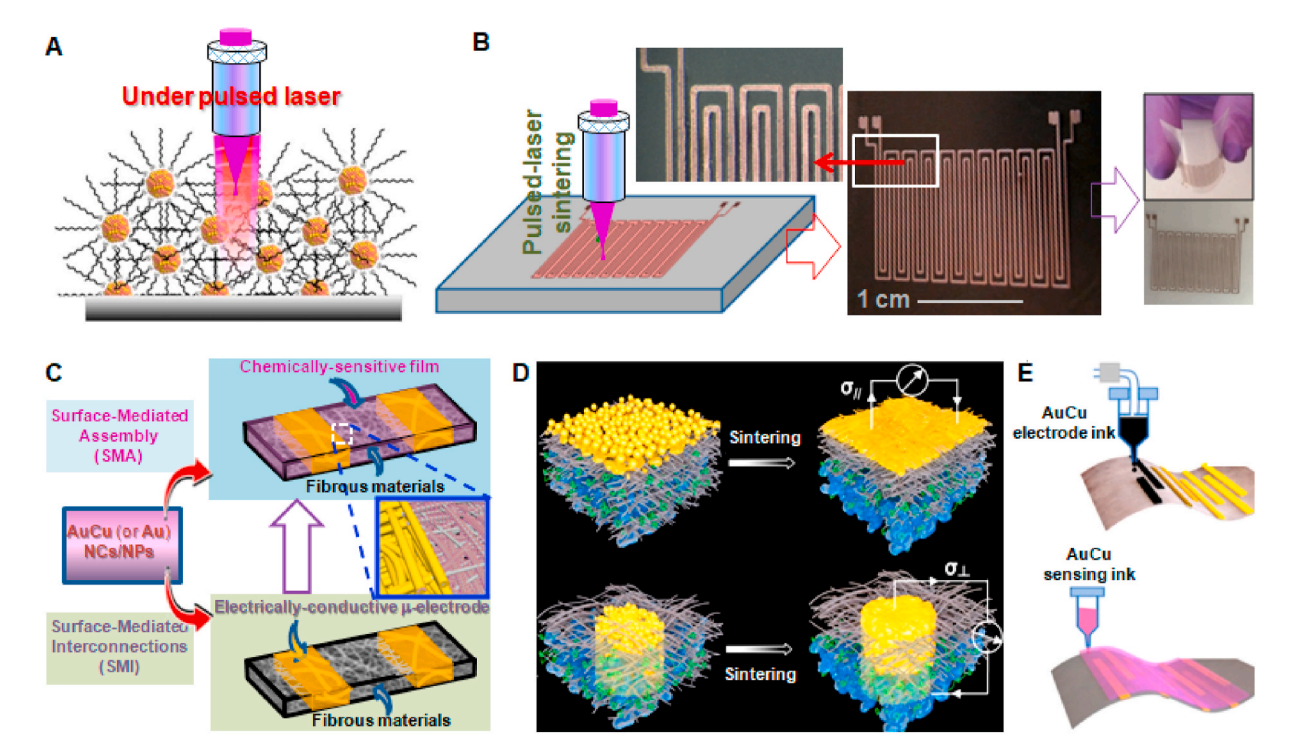


Fig. 7. Sensor fabrications: (A) Fabrication of strain sensors by nanoink-printing and pulsed-laser sintering of SANs from AuCu NPs. (B) Pulsed-laser sintering on PET substrate. Reproduced with permission (Zhao et al., 2015b) Copyright 2015 American Chemical Society. (C) SMI-SMA processes for fabrication of flexible fibrous strain sensors. (D) Illustration of the SMI-created substrate-parallel ($\sigma_{//}$) and –perpendicular conductivity (σ_{\perp}). (E) Illustration of printing microelectrodes by SMI (top) and printing sensing film by SMA (bottom). Reproduced with permission (Yan et al., 2020) Copyright 2020 Wiley-VCH.

on the different substrates. Bending fatigue test (Zhao et al., 2015b) shows that the resistance response to tensile bending exhibits a gradual increase from 2 to 20% after \sim 12,000 cycles and it returns to its initial value after a few minutes, demonstrating an excellent durability. Another intriguing example involves room-temperature sintering of AuCu NPs on fibrous and flexible substrates (Yan et al., 2020) for the fabrication of cellulosic fibrous sensor in 3D dimension. It features microelectrodes being fabricated by surface-mediated interconnection (SMI) of NPs and the sensing film being embedded by surface-mediated assembly (SMA) of NPs (Fig. 7C). It differs from conventional random interparticle necking pathways via high-temperature sintering or cold welding, which often exhibits poor adhesion to fibrous materials. The SMI pathway not only enables surface connection of atomic layers among NPs and a good adhesion and potential patternability to the fibrous materials, but also produces metallic conductivity on the surface or through the thickness of the substrate (i.e., σ_{\perp} or $\sigma_{//}$) (Fig. 7D). This approach demonstrates an electrical conductivity corresponding to 53% of bulk Cu conductivity and porosity-dependent anisotropy of electrical conductivity. The electrical resistance responses to compressive or tensile strains, and exhibits insignificant changes after multiple bending cycles. The SMI-SMA coupling allows printing a microelectrode pattern on the fibrous substrate and subsequent printing of the sensing film (Fig. 7E). This approach (Yan et al., 2020) could form the basis for a paradigm shift in the design and fabrication of 3D fibrous strain sensors.

SAN strain sensing characteristics. As stated, the strain sensing characteristics for strain sensors fabricated by polymers or graphenes/carbon nanotubes have been extensively studied, which have been covered in many recent reviews (Seyedin et al., 2019; Souri et al., 2020). Mechanistically, they involve resistive, capacitive and piezoelectric types. Table 1 shows some examples of resistive types comparing SAN strain sensors and other types of strain sensor in terms of stretchability, gauge factor, response time, and cycle stability. While there are many aspects showing that polymer-based strain sensors have clear advantages, e.g., device stretchability and durability, SAN derived strains feature molecular level and nanoscale tunabilities of the sensing characteristics.

Like other traditional strain sensors, flexible substrates, including stretchable ones, offer an effective way to manipulate the sensing characteristics, which largely rely on the changes in materials volume density as a result of tensile or compressive strains. In comparison, the changes mainly occur in response to subtle changes in interparticle spatial properties in SANs on flexible substrates in terms of tensile or compressive strains. This contrasts with SANs on rigid substrates (Cheng et al., 2018a), where the intermolecular interactions are fixed as

assembled. Differing from the sensing element in a chemical sensor, a strain or gauge sensor is grouped under strain gauge with its electrical resistance being sensitive to the force applied to the device, including pressure, tension, mass loading, etc. SAN on a flexible substrate patterned with interdigitated microelectrodes effectively integrates the chemical and strain/gauge sensing functions into one sensing element (Huynh and Haick, 2018; Wu et al., 2013). For example, SANs of Au NPs using linking molecules such as 11-mercaptoundecanoic acid (MUA), 16-mercaptohexadecanoic acid (MHA), or 1,9-nonadithiol (NDT) by interparticle hydrogen-bonding (MUA or MHA) or alkyl chain linkage (NDT) in addition to the hydrophobic interactions (Shan et al., 2014) exhibit responses to the device bending in vertical or horizontal orientation with respect to the microelectrode orientation. Such compressive strain or tensile strain produces differential resistance change ($\Delta R/R$) depending strongly on the radius of curvature in the bending direction (R_b) (Fig. 8A) (Yin et al., 2011). Indeed, $\Delta R/R$ exhibits a larger change for compressive strain than that for tensile strain. On the other hand, $\Delta R/R$ increases with R_b with opposite signs between tensile strain and compressive strain, and decreases with ε (dielectric constant). By carrying out the measurement under different vapor/gas atmosphere, the resistance change (ΔR) shows subtle differences depending on tensile and compressive strain. The resistance increases for tensile strain (positive response) and decreases for compressive strain (negative response) (Fig. 8A), which is consistent with the increase and decrease of the interparticle distance in the SAN, respectively. The absolute values in resistance change are much smaller for tensile strain than those for compressive strain. These strain-responsive characteristics exhibit not only a high sensitivity of the interparticle distance to the strains by the flexible substrate, but also a clear difference of responses between tensile and compressive strain. The responses to the "loosened" interparticle molecular interdigitation upon tensile strain are much larger than the "squeezed" interparticle molecular interdigitation upon compressive

Given the molecular/atomic level sensitivity of intermolecular interactions in an ordered 2D monolayer on planar surfaces (Seo et al., 2017), the structural characteristic of SANs is expected to provide 3D-tunable intermolecular interactions for sensing, especially on flexible or stretchable substrates. There have been many examples of the chemical/bio sensors with SAN on rigid and flexible substrates by exploiting different signal transductions (Broza et al., 2018; Kahn et al., 2015; Vishinkin and Haick, 2015; Zamborini et al., 2012). In the example of a chemiresitive sensor that operates under device strains highlighted here, SAN involves a thin-film assembly of NDT–linked Au NPs as the sensing interface (Shan et al., 2014). The interparticle linkage

Table 1Properties of selected examples of SAN-strain sensors.

SAN system	Stretchability [%]	Sensitivity/g- factor	Response time [ms]	Cycle stability	References
Ni NWs/Ecoflex	100	Up to 200	0.32	up to 2.0×10^3 cycles	Wang et al., (2018)
Au NPs/abrasive paper	0.59	Up to 75.8	20	$>1.8 \times 10^4$ cycles	Liao et al., (2017)
CNTs/Au NPs/PDMS	50	Up to 70	60	$>1.0 \times 10^4$ cycles	Luo et al., (2017)
Au NPs/PDMS	100	9.54 dB/ε	<12	$>6.0 \times 10^3$ cycles	Guo et al., (2019)
Ag NWs/PU fiber/PDMS	60	Up to 9557	120	$>1.0 \times 10^4$ cycles	Cao et al., (2018)
MPA-modified AuNP film	_	Up to 109	_	up to 7.0×10^4 cycles	Jiang et al., (2015a)
Au NPs sensing strips	_	Up to 300	_	up to 1.0×10^4 cycles	Segev-Bar et al., (2015a)
Graphene/Ag NWs	200	22.9	<1	up to 1.0×10^4 cycles	Li et al., (2016a)
Au NPs/PET	-	Up to 300	<120	-	Yi et al., (2015)
MUA/Au NPs	_	Up to 400	_	up to 1.2×10^4 cycles	Zhao et al. (2015a)
Au NPs/PDMS	_	Up to 26	_	up to 1.0×10^4 cycles	Ketelsen et al., (2018)
CdSe nanocrystals/Au NC	_	5045	_	$>1.0 \times 10^4$ cycles	Lee et al., (2017b)
Ag nanocrystal/TBAB	_	Up to 300	_	$>1.0 \times 10^3$ cycles	Lee et al., (2018)
Ag nanocrystals/MPA/EDT	_	Up to 312	_	up to 1.0×10^3 cycles	Lee et al., (2017a)
Graphene NPs/carbon blacks/wool fabric/Ecoflex	150	Up to 0.5	_	up to 1.0×10^3 cycles	Souri and Bhattacharyya (2018)
Graphene NPs/carbon blacks/cotton fabric/ Ecoflex	150	1.67–6.05	-	up to 1.0×10^3 cycles	Souri and Bhattacharyya (2018)

Abbreviations: NWs: nanowires; NPs: nanoparticles; CNTs: carbon nanotubes; PDMS: poly(dimethylsiloxane); PU: polyurethane; MPA: mercaptopropionic acid; MUA: 11-mercaptoundecanoic acid; TBAB: tetrabutylammonium bromide; EDT: 1,2-ethanedithiol.

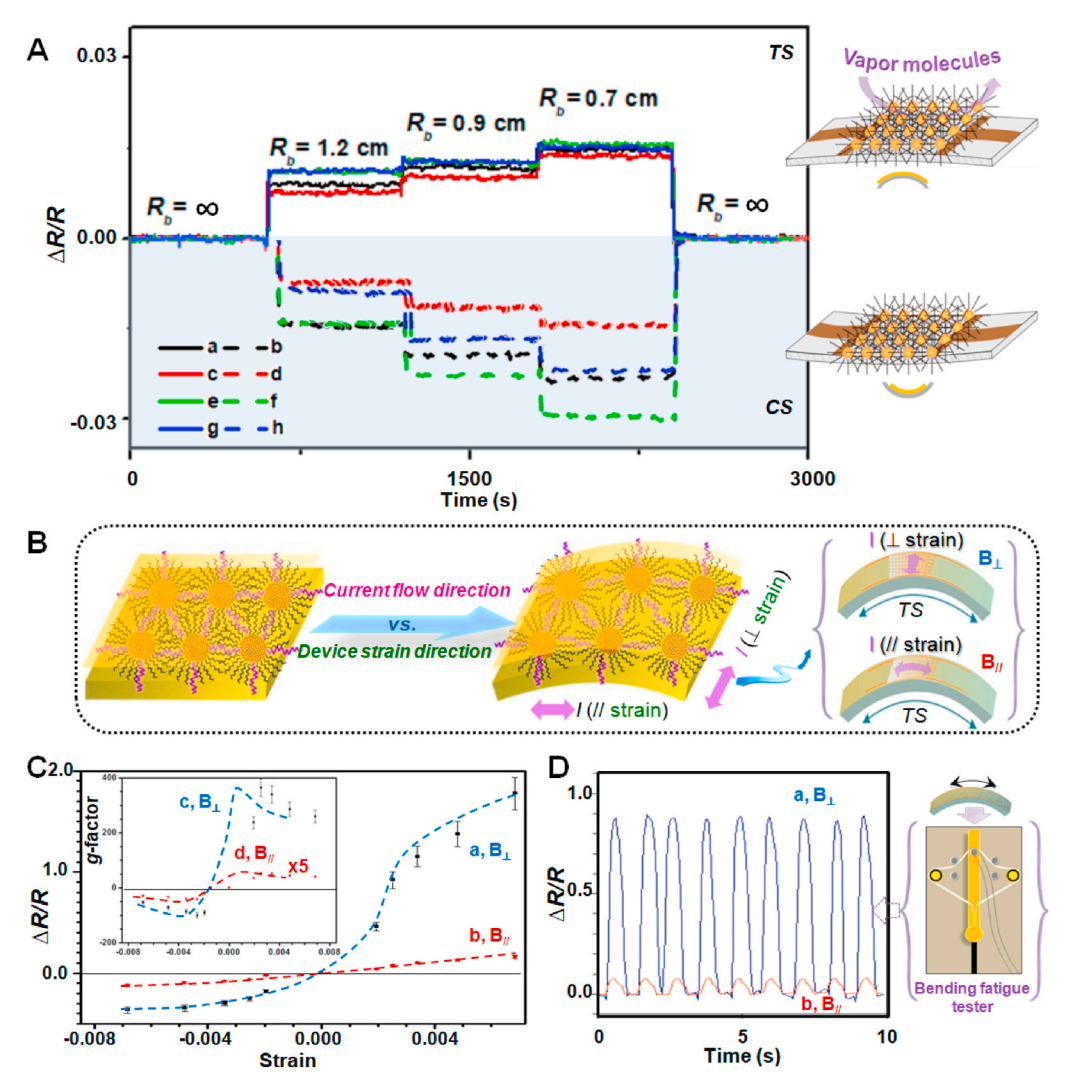


Fig. 8. Strain sensing characteristics: (A) $(\Delta R/R_{\text{flat}})$ of SAN with NDT-linked Au NPs on flexible chemiresistor in response to compressive strain (CS) and tensile strain (TS) under different Rb and atmospheres: nitrogen (a-b), ethanol (c-d), hexane (e-f), and acetone (g-h). Reproduced with permission (Shan et al., 2014) Copyright 2014 Royal Society of Chemistry. (B) SAN with MUA-linked Au NPs on a flexible chemiresistor under TS with two different bending orientations with respect to the current (I) flow direction: perpendicular to $I(B_{\perp})$, and parallel to I $(B_{//})$. (C) $\Delta R/R$ (a–b) and g-factor (c–d) in response to B₁ (a and c, black squares) and $B_{//}$ (b and d, red circles). (D) Response profiles under a repetitive strain cycles of B_{\perp} (a) and $B_{//}$ (b) using a bending fatigue tester (inset). Reproduced with permission (Zhao et al., 2015a) Copyright 2015 Wiley-VCH. (For interpretation of the references to colour in this figure legend, the reader is referred to the Web version of this article.)

of NDT involves Au(I)-thiolate chemistry at both ends of the alkyl chain in addition to the cohesive interaction of the capping alkanethiolate molecules. As shown in Fig. 8A, the resistance increases under tensile strain, in contrast to the resistance decrease under compressive strain. The magnitude of the response depends on the chemical nature of the vapor molecules and the direction of the strain. Theoretically, the change of resistance can be described by the change in interparticle distance, which increases in the case of tensile strain and decreases in the case of compressive strain. The overall response to the sorption of vapor molecules in the SAN reflects a combination of the interparticle properties and device strain characteristics. Compressive strain or tensile strain can be easily introduced to the assembly on a flexible microelectrode sensor device, leading to responses to R_b for the flexible device. Under a given R_b , the differential resistance changes ($\Delta R/R$) under compressive and tensile strain can be expressed as $\Delta R/R_{\rm flat} =$ $(R_{\text{(tensile or compressive strain)}} - R_{\text{flat}})/R_{\text{flat}}$, where $R_{\text{(tensile or compressive strain)}}$ (Yin et al., 2011) depends on $\varepsilon_{\text{strain}}$. Under different device strains (i.e., $R_{\rm b}$ in tensile or compressive strain), the flexible sensor is shown to be responsive to exposures to different vapor molecules with subtle differences in molecular polarity, hydrophobicity, hydrophilicity, and dielectric properties.

For the SAN with NDT-linked Au NPs under different device strains in the presence of different vapor molecules, the magnitude of the response sensitivity exhibits the order of ethanol > hexane > acetone, demonstrating its sensitivity to molecular interactions in the SAN (Shan et al., 2014). While the strain effect is clearly overpowered by the

relative change in resistance in response to the vapor sorption in the tested concentration range, the results have demonstrated the viability of the same sensing interface with dual sensing functions, which has implications for controlling the strain tolerance under different conformal or bending environments.

The dependence of strain response, or gauge factor (g-factor), on the strain orientation is another intriguing characteristic of SAN. Consider, for example, the case of tensile strain in terms of device bending degree and orientation with respect to the current flow direction (I) across the interdigitated microelectrode array on flexible PET (polyethylene terephthalate) substrate (Fig. 8B). The magnitude of the chemiresistive response is shown in Fig. 8C in terms of $\Delta R/R$ and g-factor (inset) for a SAN with MUA-linked Au NPs as a function of strain in $B_{//}$ or B_{\perp} orientations. It is evident that the values of $\Delta R/R$ and g are much greater for B_{\perp} than those for $B_{//}$, by a factor of 30–40 for tensile strain and 10–20 for compressive strain. This anisotropic characteristic also depends on the size of Au NPs. For example, the magnitude of the strain responses for the SAN with 2-nm Au NPs exhibits a maximum g-value as high as 400 under tensile strain and 100 under compressive strain, which is 2-3 times greater than those for the SAN with 5-nm Au NPs (Zhao et al., 2015a). This observation seems unusual initially since g-factor would be greater for B_{//} than that for B_| simply based on the gap change between the interdigitated microelectrodes under the SAN. However, the anisotropic characteristic in this example shows that the g-factor is much larger for B_{\perp} than that for $B_{//}$ for the SAN with MUA-linked Au NPs (2 nm) (Fig. 8C-D). Under $B_{//}$ or B_{\perp} with different strains, the data exhibit the positive responses for tensile strain and negative ones for compressive strain. The fact that the magnitude of g-factor for B_\perp is much greater than those for $B_{//}$ endures repetitive strain cycles. Understanding of the high and anisotropic g-factors based on percolation theory in terms of volume fraction of the metals with long-range connectivity could shine some light into the significance of NP size, interparticle gap, and structure of the linking molecules.

4. Strain sensors for wearable applications

Harnessing interparticle spatial properties in SANs with Au or alloy NPs represents one of the emerging pathways to build strain/gauge sensors for wearable applications. Fig. 9 shows an example of applications of the gold nanoparticle assembly for wearable sensors (Ketelsen et al., 2018; Lee et al., 2017b), including strain gauge wearable sensors based on metallic Au and insulating cadmium selenide (CdSe) nanocrystal heterostructures (Lee et al., 2017b), and gauge sensors derived from cross-linked gold nanoparticles (Ketelsen et al., 2018). The first example explores the creation of nanocrystal heterostructure thin films using metallic Au nanocrystals and insulating CdSe quantum dots via 1, 2-ethanedithiol (EDT) + tetra-*n*-butylammonium bromide (TBAB) ligand exchange solution to produce highly sensitive strain gauges for wearable sensors (Lee et al., 2017b). There is an enhancement of the strain sensitivity at close to the percolation threshold in terms of the site percolation theory by the creation of nanocracks. A g-factor as high as 5000 was demonstrated, which was recorded as the highest value among nanocracks-based strain gauge sensors (Lee et al., 2017b). The construction of such strain gauge sensor in arrays showed promises as electronic skin or wearable devices in monitoring motions of finger joints, pulses of heart rate, and movements of human vocal cords. For multiarray strain wearable sensors (Fig. 9A-B), the SAN with 77% CdSe NPs hybrid with Au NPs functions as active sensing layers, whereas the SAN with TBAB-treated Ag NPs serves as electrodes by standard photolithography patterning on PET substrates (Fig. 9A). The Au-CdSe NP hybrid thin films were deposited by ligand exchange with EDT. The multiarray sensors are positioned on the joints of human fingers to detect finger bending in response to finger motions by monitoring their resistance changes (Fig. 9A-B). The sensing layers' resistance changes demonstrate the highly selective strain sensing ability. These strain sensors also showed potential use in pulse monitoring by mounting it on a waist, and in sound recording by attaching it on the neck to capture subtle skin movement during speaking. The finding demonstrated the potential of harnessing the interparticle spatial properties in SAN-derived heterostructures toward electronic skins. In addition to high g-factor, the strain sensors are shown to exhibit high durability, frequency stability, and negligible hysteresis (Lee et al., 2017b). The origin of the sensor's high sensitivity is explained by site and bond percolation theory. The sensor's high durability over 10,000 cycles for a wide range of frequencies (0.006–10 Hz) with negligible hysteresis demonstrated its viability for measuring finger joint motion, heart rate, and human vocal cords movements.

SAN-Au strain sensors. In another application, strain gauges were created by poly(dimethylsiloxane) (PDMS) contact printing of crosslinked Au NPs prepared by 1,9-nonanedithiol (NDT) cross-linking and layer-by-layer (LbL) spin coating onto flexible polyimide foil substrate (Ketelsen et al., 2018) (Fig. 9C-E). The sensors attached to the skin above the radial artery can be used for monitoring pulse waves from the muscle movements. PDMS adapts conformally to the skin and its low elastic modulus allows easy stretching. Interdigitated silver electrodes were created by dispenser printing of silver paste. A SAN with cross-linked Au NP film was prepared via LbL spin coating on a glass substrate. By pressing PDMS with pre-embedded silver paste electrodes onto the SAN and slowly removing, a PDMS supported Au NP film sensor is fabricated (Fig. 9C). Taping the sensor onto the skin above the radial artery produces a sequence of pulse wave signals (Fig. 9D). The sensor response speed and sensitivity provide diagnostic pulse wave characteristics (Fig. 9E). The deformation sensitivity of the PDMS supported strain gauges is 2 orders of magnitude higher than that of the polyimide supported sensors.

This finding has demonstrated the excellent potential of harnessing the interparticle spatial properties in SANs for constructing healthcare sensors. The sensor is also shown to exhibit linear response characteristics with g-factors from 14 to 26 depending on Au nanoparticle size (4–7 nm), which reflects the increased perturbation of interparticle charge tunneling with increasing particle size (Ketelsen et al., 2018). The strain-resistance performance remained unchanged after 10,000 strain/relaxation cycles. Such sensors are applicable to monitoring muscle movements and recording of pulse waves.

SAN-Ag NP strain sensors. Another important pathway to build strain/gauge sensors for wearable applications involves harnessing the

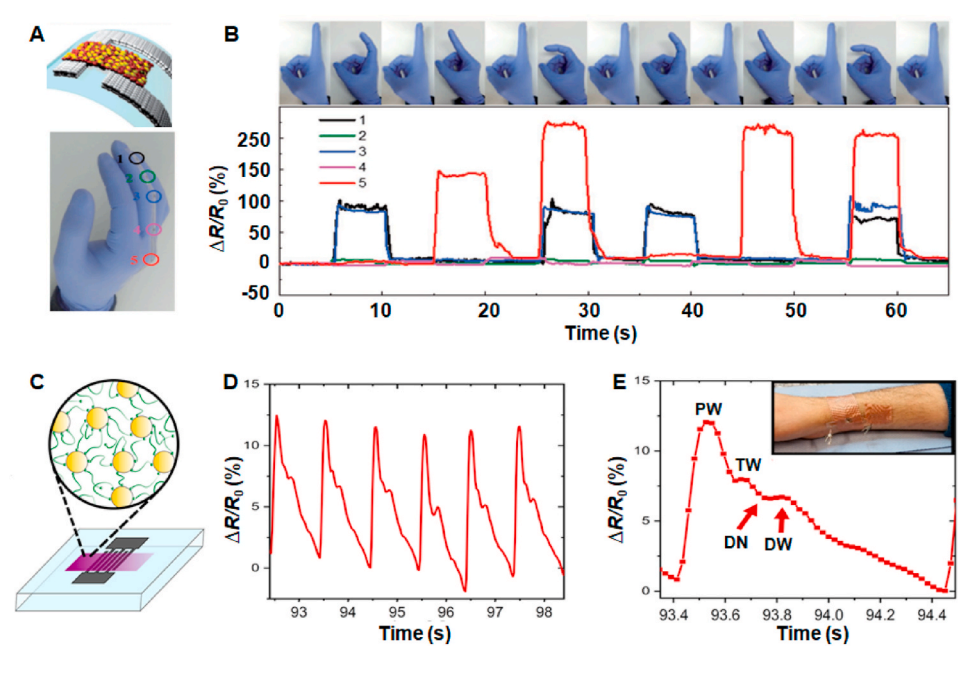


Fig. 9. Wearable strain sensors. Strain gauge sensors based on a heterostructure from metallic Au NPs in combination with insulating CdSe nanocrystals: (A) fabrication of a multiarray sensor device (top) and photo showing strain sensor on the middle finger (bottom); (B) photos showing strain sensor on the finger under various bending motions (top), and sensing performance at each motion (bottom). Reproduced with permission (Lee et al., 2017b) Copyright 2017 Wiley-VCH. Strain gauge sensor fabricated by SAN using 1,9-nonanedithiol cross-linked Au NPs films: (C) illustration of the fabricated pulse wave sensor; (D-E) the pulse waves and the well-resolved percussion wave (PW), tidal wave (TW), dicrotic notch (DN), and dicrotic wave (DW). Inset: the sensor taped to the wrist under a sampling rate of 49 Hz. Reproduced with permission (Ketelsen et al., 2018) Copyright 2018 American Chemical Society.

interparticle spatial properties in SANs with Ag NPs. Fig. 10(A-C) shows an example of such nanoparticle assemblies for strain sensor applications (Lee et al., 2017a, 2018), including wearable sensors based on transition states of SAN with Ag NPs derived by ligand-exchange processes (Lee et al., 2018), and strain sensor arrays of silver nanocrystals (Lee et al., 2017a). In one example, the transition states in the SAN with Ag NPs formed by ligand-exchange processes are exploited for potential applications as a wearable sensor to detect human motion, such as finger or neck muscle movement (Lee et al., 2018). The transition state with partially exchanged ligands shows intriguing electromechanical features (Fig. 10A) with a g-factor as high as 300, the origin of which is explained by formation of nanocracks and metal-insulator transition. A higher degree of ligand-exchange exhibits a low resistivity and g-factor, whereas a lower degree enables a high sensitivity. The strain sensor device is attached to the finger, and the resistance change is monitored upon bending and extension of the finger (Fig. 10B-C). It shows a reversible and stable resistance change upon placing on the skin of the neck. The response sensitivity, reliability, and stability (Lee et al., 2018) are demonstrated by observing linear change in resistance vs. strain, reversible and rapid return of the resistance to its original value upon strain removal, and stable change and recovery without any hysteresis during cycling. The detection of small muscle motions (e.g., swallowing movement) further highlights the significance of harnessing the interparticle spatial properties in SANs for strain/gauge sensor applications.

In another example, arrays of SANs are prepared by solution processing of Ag NPs and control of the surface ligand chemistry, which are demonstrated for fabricating wearable multi-array strain sensor systems to detect human wrist motion (Fig. 10D) (Lee et al., 2017a). The strain-sensitive part of the SAN is prepared by EDT or MPA (3-mercaptopropionic acid) ligand exchange on Ag NPs. The strain-insensitive part is created as conductive electrodes by Br or Cl treatment of Ag NPs. Both function as building blocks to construct strain sensor devices. The electromechanical properties of the SAN with Ag NPs are sensitive to the strain, showing g-factors up to 312. The multi-sensor arrays have demonstrated the viability for use as electronic skins. With the integration of Ag NPs in the sensing layers and electrodes into one device, the resistance showed reversible changes to given strains (Fig. 10D). By attaching the device on the human wrist (Fig. 10E), the bending up and

down produces compressive and tensile strains, exhibiting negative and positive changes in resistance, respectively (Fig. 10F). The high sensitivity of the wearable sensor in capturing the motion of the wrist shows potential applications in electronic skin, highlighting the significance of harnessing interparticle spatial properties in constructing strain sensors.

Comparisons of different types of strain sensors. It is evident that SAN-based strain sensors have found a wide range of applications in wearable sensors, which parallel some of the earlier stages of wearable applications for polymer and graphenes/carbon nanotubes-based strain sensors. This is indeed shown by the applications of the strain sensors based on different sensing materials and sensing mechanisms such as piezoelectric and triboelectric strain sensors, both of which are selfpowered. The applications are covered in many recent reviews (Chen et al., 2021; Chen and Wang, 2017; Huynh and Haick, 2018; Niu et al., 2019; Oh and Bao, 2019; Seyedin et al., 2019; Souri et al., 2020; Tat et al., 2021; Zhang et al., 2017b, 2021). As the SAN research and development continue to reveal new structures and properties, new opportunities are emerging in exploring the properties of different SAN strain sensors including strain sensors constructed from different types of multifunctional nanoparticles and ligands, and strain sensors that can be used for making body sensor networks. Fig. 11 outlines some of the emerging opportunities and directions for the expansion of SAN strain

In contrast to traditional strain sensors, the SAN-derived strain sensors also offer the advantage of configuring multifunctional sensors by incorporating chemical/bio sensitivity into strain sensitivity. This was indeed demonstrated for SAN-derived sensors on flexible substrates, including alkyl dithiols linked assembly of gold nanoparticles on PET substrates (Shan et al., 2014) and dendrons derivatized thiols linked assembly of gold nanoparticles on paper substrates (Yan et al., 2017).

5. Conclusions and future perspectives

In conclusion, harnessing the interparticle spatial properties of SANs is an intriguing pathway for the design of strain/gauge sensors, which is transformative and versatile in terms of creating the strain-sensitive components at the nanoscale and molecular levels, and the small quantiles of nanoparticles. Such nanoparticles are not only easily

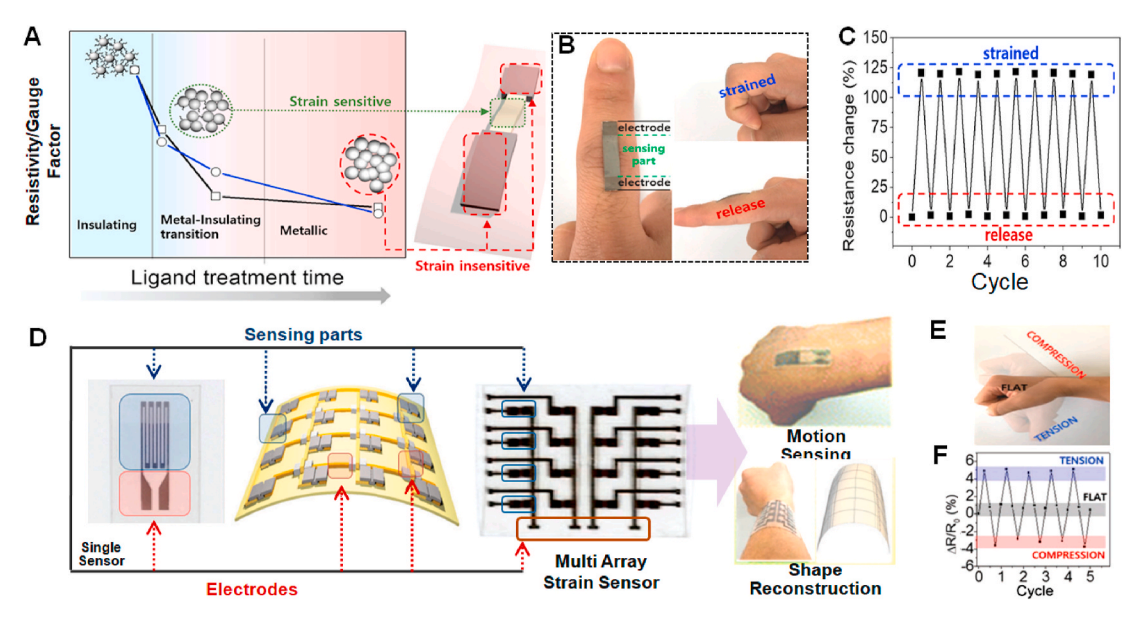


Fig. 10. Wearable strain sensors. Sensors fabricated by controlling the transition states for a SAN with Ag NPs formed during ligand-exchange processes: (A) illustration of the resistivity/g-factor vs. ligand-exchange time, (B-C) photos showing a strain sensor attached to a finger under strain and release motion (B), and resistance change during finger bending (C). Reproduced with permission (Lee et al., 2018) Copyright 2018 American Chemical Society. Strain sensor arrays of Ag NC: (D) fabrication process of the sensor, (E–F) photos showing wrist motion with strain sensor (E), and resistance change during bending cycles for the wrist with a strain sensor (F). Reproduced with permission (Lee et al., 2017a) Copyright 2017 Royal Society of Chemistry.

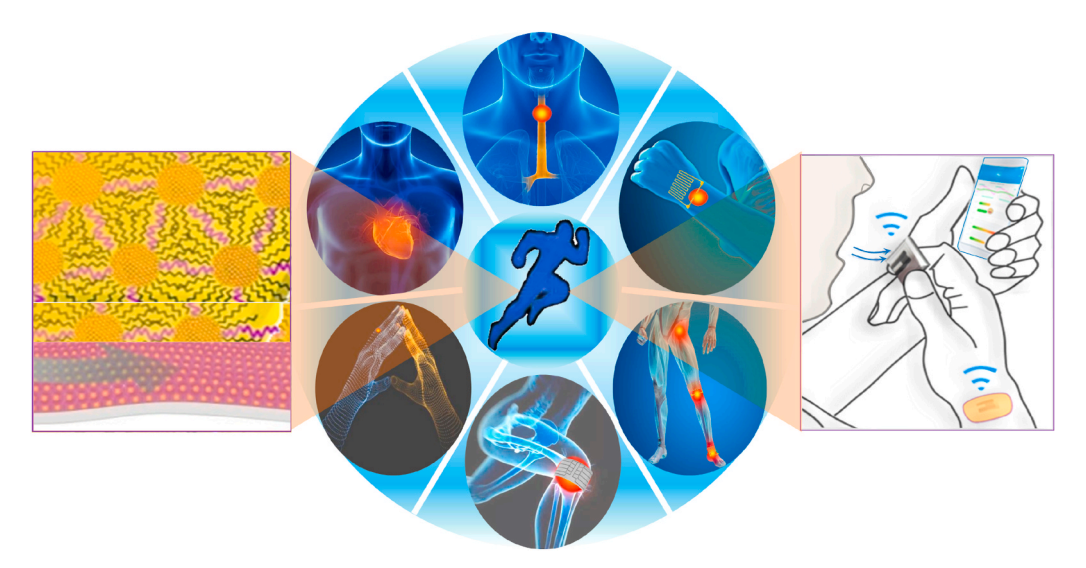


Fig. 11. Nanoengineering SANs and exploring future opportunities in wearable biosensors and bioelectronics.

synthesized, but also highly tunable in terms of size, shape, and composition. The subtle differences in materials and structures utilized for constructing SANs exhibit profound influences on the detailed sensing characteristics in terms of sensitivity, range, and hysteresis. In comparison with traditional approaches in fabricating strain gauge sensors largely based on a single conductive beam pattern, the major advantages of SAN-based strain sensors include high sensitivity, broad range and minimized hysteresis. These sensing characteristics are tunable by a combination of interparticle spatial properties and nanoparticle sizes and shapes.

For SAN based sensors, a key challenge for future research and development is the understanding of factors controlling the structural durability and stretchability for wearable applications. The potentially limited stability of the materials used for some SANs under repetitive device bending must be further investigated. Addressing this challenge requires understanding of defects caused by weak adhesion of SAN to substrate, background resistance drifting, oxidation of nanoparticles, and irreversible cracks in the film, etc. The chemical nature of the metal, e.g., Au, Ag, and Cu, for the nanoparticles must also be considered. While the cost of Ag or Cu is lower than Au, the propensity of oxidation of Cu and Ag, and the releasing of Ag ion species in the films under high humidity conditions is yet to be addressed. Moreover, in-depth fundamental understanding of the detailed relationships between the nanostructure strain and electrical properties will shape the future development of wearable sensors and electronic skins in several significant fronts. The nanostructure defined by the combination of metal nanoparticles and interparticle molecules provides a paradigm shift in the design of sensitive materials in terms of the intermolecular interaction tunability and the electrical sensing signal transduction. The recent intensification of interests in wearable strain sensors stems from the ability of conformal device incorporation onto the human body. One area involves the exploration of human-friendly paper substrates with deformability and biocompatibility on human skin for the fabrication of SAN based sensors. The explorations of the interparticle spatial properties of SANs on flat, flexible or curved surfaces are expected lead to a wide range of applications in wearable and skin electronics. Another challenging question is how to optimize the combination of the nanoengineered particles and the structurally-tunable molecules in the flexible electronics configurations. In addition to continuing refinements of the parameters in the traditional wet chemistry syntheses, other solventfree methods, such as electron beam or dose-controlled formation and assembly of nanoclusters and nanoparticles from aurophilic ensembles on a substrate surface (Cheng et al., 2018a, 2018b), could also be exploited to enable the control over dimensionality of the nanoparticle assembly.

There is a clear need of further studies of the performance dependences on the sizes and geometries of the nanoparticles. The particle size effect is manifested not only in the planar-to-curved transition for the van der Waals interaction within self-assembled monolayers (Cometto et al., 2017), but also in the interparticle spatial conformation. In the theoretical modeling front, computational modeling of the interparticle molecular interactions in correlation to the overall SAN's elasticity in terms of Young's moduli and conductive percolation is needed. Molecular dynamics simulations of the interparticle spatial structures of SAN before and after the tensile or compressive strains (Li et al., 2017) could perhaps provide some important insight into the strain sensor sensitivity and durability, especially under bending fatigue conditions. Another direction involves optimization of the nanocomposites by tuning the capping/linking molecules in terms of ordered/disordered packing structures of alkyl chains (Cheng et al., 2019), dendritic macromolecules (Yan et al., 2017), or 1D assembly of nanoparticles by electron dosing (Cheng et al., 2018b), in combination with fibrous materials as the substrate matrix (Cheng et al., 2017; Kang et al., 2016; Yan et al., 2017, 2020). Exploring the synergy of these nanocomposite structures in strain sensing requires a further understanding of the control factors governing the formation of SANs on different surfaces or substrates in terms of adhesion to the substrate, which may lead to a wide range of wearable sensor applications. An important challenge for future research front of SAN sensors is thus the development of the ability to control the formation of SANs on different substrates in terms of the specific phase or composite structures, the SAN - substrate interactions (adhesion), and the long-term performance durability under wearable applications. Some of the recent strategies to the tunable nanoparticle assemblies (Song et al., 2020) include air-liquid, liquid-liquid, and air-liquid-liquid interfacial assembling routes, and functionalization or composite formation of the nanoparticle assemblies to enhance the stability, stretchability and conductivity.

Declaration of competing interest

The authors declare that they have no known competing financial interests or personal relationships that could have appeared to influence the work reported in this paper.

Acknowledgement

This work was supported by the National Science Foundation (IIP 1640669), USA, and the NNSFC (Grant no. 31800830), China.

Binghamton University Integrated Electronics Engineering Center (IEEC) is also acknowledged for partial support of the work.

References

- Bae, G.Y., Han, J.T., Lee, G., Lee, S., Kim, S.W., Park, S., Kwon, J., Jung, S., Cho, K., 2018. Adv. Mater 30 (43), 1803388.
- Baghbanzadeh, M., Bowers, C.M., Rappoport, D., Zaba, T., Yuan, L., Kang, K., Liao, K.C., Gonidec, M., Rothemund, P., Cyganik, P., Aspuru-Guzik, A., Whitesides, G.M., 2017. J. Am. Chem. Soc. 139 (22), 7624-7631.
- Broza, Y.Y., Vishinkin, R., Barash, O., Nakhleh, M.K., Haick, H., 2018. Chem. Soc. Rev. 47 (13), 4781-4859.
- Cao, Z., Wang, R., He, T., Xu, F., Sun, J., 2018. ACS Appl. Mater. Interfaces 10 (16), 14087_14096
- Casalini, S., Bortolotti, C.A., Leonardi, F., Biscarini, F., 2017. Chem. Soc. Rev. 46 (1), 40-71
- Casanova-Cháfer, J., Bittencourt, C., Llobet, E., 2019. Beilstein J. Nanotechnol. 10, 565-577
- Chen, J., Wang, Z.L., 2017. Joule 1 (3), 480-521.
- Chen, J., Chang, B., Oyola-Reynoso, S., Wang, Z., Thuo, M., 2017. ACS Omega 2 (5), 2072_2084
- Chen, G., Au, C., Chen, J., 2021. Trends Biotechnol. https://doi.org/10.1016/j. tibtech.2020.12.011.
- Cheng, H.W., Yan, S., Han, L., Chen, Y., Kang, N., Skeete, Z., Luo, J., Zhong, C.J., 2017. Nanoscale 9 (11), 4013-4023.
- Cheng, H.W., Wang, J., Li, Y.J., Li, J., Yan, S., Shan, S., Wang, L., Skeete, Z., Zhong, C.J., 2018a. Small 14 (20), 1800598.
- Cheng, H.W., Yan, S., Li, J., Wang, J., Wang, L., Skeete, Z., Shan, S., Zhong, C.J., 2018b. ACS Appl. Mater. Interfaces 10 (46), 40348-40357.
- Cheng, H.W., Wu, Z.P., Yan, S., Li, J., Shan, S., Wang, L., Porter, M.D., Zhong, C.J., 2019. Chem. Sci. 10 (29), 7104-7110.
- Cheng, H.W., Wang, S., Porter, M.D., Zhong, C.J., 2021. Chem. Sci. https://doi.org/ 10.1039/d0sc06955h
- Chun, S., Son, W., Kim, H., Lim, S.K., Pang, C., Choi, C., 2019. Nano Lett. 19 (5), 3305-3312.
- Colangelo, E., Comenge, J., Paramelle, D., Volk, M., Chen, Q., Lévy, R., 2017. Bioconjugate Chem. 28 (1), 11-22.
- Cometto, F.P., Luo, Z., Zhao, S., Olmos-Asar, J.A., Mariscal, M.M., Ong, Q., Kern, K., Stellacci, F., Lingenfelder, M., 2017. Angew. Chem. Int. Ed. 56 (52), 16526-16530.
- Dinh, T., Nguyen, T., Phan, H.P., Nguyen, N.T., Dao, D.V., Bell, J., 2020. Biosens. Bioelectron 166, 112460.
- Gao, Y., Ota, H., Schaler, E.W., Chen, K., Zhao, A., Gao, W., Fahad, H.M., Leng, Y. Zheng, A., Xiong, F., Zhang, C., Tai, L.C., Zhao, P., Fearing, R.S., Javey, A., 2017. Adv. Mater 29 (39), 1701985.
- Guo, J., Zhou, B., Zong, R., Pan, L., Li, X., Yu, X., Yang, C., Kong, L., Dai, Q., 2019. ACS Appl. Mater. Interfaces 11 (37), 33589-33598.
- Herrmann, J., Müller, K.H., Reda, T., Baxter, G.R., Raguse, B., de Groot, G.J.J.B., Chai, R., Roberts, M., Wieczorek, L., 2007. Appl. Phys. Lett. 91 (18), 183105.
- Ho, M.D., Ling, Y., Yap, L.W., Wang, Y., Dong, D., Zhao, Y., Cheng, W., 2017. Adv. Funct. Mater. 27 (25), 1700845.
- Hostetler, M.J., Wingate, J.E., Zhong, C.J., Harris, J.E., Vachet, R.W., Clark, M.R., Londono, J.D., Green, S.J., Stokes, J.J., Wignall, G.D., Glish, G.L., Porter, M.D., Evans, N.D., Murray, R.W., 1998. Langmuir 14 (1), 17-30.
- Hua, Q., Sun, J., Liu, H., Bao, R., Yu, R., Zhai, J., Pan, C., Wang, Z.L., 2018. Nat. Commun 9 (1), 244.
- Huynh, T.P., Haick, H., 2018. Adv. Sci. 30 (50), 1802337.
- Jiang, C.W., Ni, I.C., Tzeng, S.D., Kuo, W., 2015a. Sci. Rep. 5, 11939.
- Jiang, L., Sangeeth, C.S., Nijhuis, C.A., 2015b. J. Am. Chem. Soc. 137 (33), 10659-10667.
- Jin, R.C., Zeng, C.J., Zhou, M., Chen, Y.X., 2016. Chem. Rev. 116 (18), 10346-10413. Kahn, N., Lavie, O., Paz, M., Segev, Y., Haick, H., 2015. Nano Lett. 15 (10), 7023-7028.
- Kang, N., Lin, F., Zhao, W., Lombardi, J.P., Almihdhar, M., Liu, K., Yan, S., Kim, J., Luo, J., Hsiao, B.S., Poliks, M., Zhong, C.J., 2016. ACS Sens. 1 (8), 1060-1069.
- Ketelsen, B., Yesilmen, M., Schlicke, H., Noei, H., Su, C.H., Liao, Y.C., Vossmeyer, T., 2018. ACS Appl. Mater. Interfaces 10 (43), 37374-37385.
- Khoshmanesh, F., Thurgood, P., Pirogova, E., Nahavandi, S., Baratchi, S., 2021. Biosens. Bioelectron 176, 112946.
- Kong, G.D., Kim, M., Cho, S.J., Yoon, H.J., 2016. Angew. Chem., Int. Ed. 55 (35), 10307-10311.
- Kong, G.D., Jin, J., Thuo, M.M., Song, H., Joung, J.F., Park, S., Yoon, H.J., 2018. J. Am. Chem. Soc. 140 (38), 12303-12307.
- Lee, S.W., Joh, H., Seong, M., Lee, W.S., Choi, J.H., Oh, S.J., 2017a. J. Mater. Chem. C 5 (9), 2442-2450.
- Lee, W.S., Lee, S.W., Joh, H., Seong, M., Kim, H., Kang, M.S., Cho, K.H., Sung, Y.M., Oh, S.J., 2017b. Small 13 (47), 1702534.
- Lee, S.W., Joh, H., Seong, M., Lee, W.S., Choi, J.H., Oh, S.J., 2018. ACS Appl. Mater. Interfaces 10 (30), 25502-25510.
- Li, Q., Ullah, Z., Li, W.W., Guo, Y.F., Xu, J.B., Wang, R.B., Zeng, Q., Chen, M.L., Liu, C.J., Liu, L.W., 2016a. Small 12 (36), 5058-5065.
- Li, X., Yang, T., Yang, Y., Zhu, J., Li, L., Alam, F.E., Li, X., Wang, K., Cheng, H., Lin, C.T., Fang, Y., Zhu, H., 2016b. Adv. Funct. Mater. 26 (9), 1322-1329.
- Li, B., Bian, K., Lane, J.M.D., Salerno, K.M., Grest, G.S., Ao, T., Hickman, R., Wise, J., Wang, Z., Fan, H., 2017. Nat. Commun 8, 14778.
- Liao, X., Zhang, Z., Liang, Q., Liao, Q., Zhang, Y., 2017. ACS Appl. Mater. Interfaces 9 (4), 4151-4158.

- Lim, S., Zhong, C.J., 2009. Acc. Chem. Res. 42 (6), 798-808.
- Love, J.C., Estroff, L.A., Kriebel, J.K., Nuzzo, R.G., Whitesides, G.M., 2005. Chem. Rev. 105 (4), 1103–1169.
- Lu, Y., Biswas, M.C., Guo, Z., Jeon, J.W., Wujcik, E.K., 2019. Biosens. Bioelectron 123,
- Luo, C., Jia, J., Gong, Y., Wang, Z., Fu, Q., Pan, C., 2017. ACS Appl. Mater. Interfaces 9 (23), 19955–19962.
- Meng, K., Zhao, S., Zhou, Y., Wu, Y., Zhang, S., He, Q., Wang, X., Zhou, Z., Fan, W., Tan, X., Yang, J., Chen, J., 2020. Matter 2 (4), 896-907.
- Newcomb, L.B., Tevis, I.D., Atkinson, M.B., Gathiaka, S.M., Luna, R.E., Thuo, M., 2014. Langmuir 30 (40), 11985-11992.
- Niu, S., Matsuhisa, N., Beker, L., Li, J., Wang, S., Wang, J., Jiang, Y., Yan, X., Yun, Y., Burnett, W., Poon, A.S.Y., Tok, J.B.H., Chen, X., Bao, Z., 2019. Nat. Electron 2, 361-368.
- Oh, J.Y., Bao, Z., 2019. Adv. Sci. 6 (11), 1900186.
- Olichwer, N., Meyer, A., Yesilmen, M., Vossmeyer, T., 2016. J. Mater. Chem. C 4 (35), 8214-8225.
- Park, D.Y., Joe, D.J., Kim, D.H., Park, H., Han, J.H., Jeong, C.K., Park, H., Park, J.G., Joung, B., Lee, K.J., 2017. Adv. Mater 29 (37), 1702308.
- Sangeetha, N.M., Decorde, N., Viallet, B., Viau, G., Ressier, L., 2013. J. Phys. Chem. C 117 (4), 1935–1940.
- Segev-Bar, M., Konvalina, G., Haick, H., 2015a. Adv. Mater 27 (10), 1779-1784. Segev-Bar, M., Ukrainsky, B., Konvalina, G., Haick, H., 2015b. J. Phys. Chem. C 119 (49),
- 27521-27528 Seo, S., Hwang, E., Cho, Y., Lee, J., Lee, H., 2017. Angew. Chem. Int. Ed. 56 (40), 12122-12126.
- Seyedin, S., Zhang, P., Naebe, M., Qin, S., Chen, J., Wang, X., Razal, J.M., 2019. Mater. Horiz 6, 219-249.
- Shan, S., Zhao, W., Luo, J., Yin, J., Switzer, J.C., Joeseph, P., Lu, S., Poliks, M., Zhong, C. J., 2014. J. Mater. Chem. C 2 (10), 1893-1903.
- Someya, T., Bao, Z., Malliaras, G.G., 2016. Nature 540 (7633), 379-385.
- Song, P., Yuan, L., Roemer, M., Jiang, L., Nijhuis, C.A., 2016. J. Am. Chem. Soc. 138 (18), 5769-5772
- Song, L., Huang, Y., Nie, Z., Chen, T., 2020. Nanoscale 12 (14), 7433-7460.
- Souri, H., Bhattacharyya, D., 2018. ACS Appl. Mater. Interfaces 10 (24), 20845–20853. Souri, H., Banerjee, H., Jusufi, A., Radacsi, N., Stokes, A.A., Park, I., Sitti, M., Amjadi, M., 2020. Adv. Intell. Syst 2 (8), 2000039.
- Tat, T., Libanori, A., Au, C., Yau, A., Chen, J., 2021. Biosens. Bioelectron 171, 112714. Thompson, D., Nijhuis, C.A., 2016. Acc. Chem. Res. 49 (10), 2061–2069.
- Vishinkin, R., Haick, H., 2015. Small 11 (46), 6142-6164.
- Wang, G.R., Wang, L., Rendeng, Q., Wang, J., Luo, J., Zhong, C.J., 2007a. J. Mater. Chem. 17 (5), 457–462.
- Wang, L., Shi, X., Kariuki, N.N., Schadt, M., Wang, G.R., Rendeng, Q., Choi, J., Luo, J., Lu, S., Zhong, C.J., 2007b. J. Am. Chem. Soc. 129 (7), 2161-2170.
- Wang, L., Luo, J., Schadt, M.J., Zhong, C.J., 2010. Langmuir 26 (2), 618-632.
- Wang, C., Li, X., Gao, E.L., Jian, M.Q., Xia, K.L., Wang, Q., Xu, Z.P., Ren, T.L., Zhang, Y. Y., 2016. Adv. Mater 28 (31), 6640-6648.
- Wang, S., Chen, K., Wang, M., Li, H., Chen, G., Liu, J., Xu, L., Jian, Y., Meng, C., Zheng, X., Liu, S., Yin, C., Wang, Z., Du, P., Qu, S., Leung, C.W., 2018. J. Mater. Chem. C 6 (17), 4737-4745.
- Wei, Y., Chen, S., Yuan, X., Wang, P., Liu, L., 2016. Adv. Funct. Mater. 26 (28), 5078-5085
- Wu, W.Z., Wen, X.N., Wang, Z.L., 2013. Science 340 (6135), 952–957.
- Wu, X., Han, Y., Zhang, X., Zhou, Z., Lu, C., 2016. Adv. Funct. Mater. 26 (34), 6246-6256.
- Xiang, D., Wang, X., Jia, C., Lee, T., Guo, X., 2016. Chem. Rev. 116 (7), 4318-4440. Yan, S., Liu, X., Skeete, Z., He, N., Xie, Z.H., Zhao, W., Lombardi III, J.P., Liu, K., Kang, N., Luo, J., Hsiao, B.S., Poliks, M., Gitsov, I., Zhong, C.J., 2017. Adv. Mater. Interfaces 4 (22), 1700380-1700391.
- Yan, S., Shan, S., Wen, J., Li, J., Kang, N., Wu, Z., Lombardi, J., Cheng, H.W., Wang, J., Luo, J., Mott, N.D., Wang, L., Ge, Q., Hsiao, B.S., Poliks, M., Zhong, C.J., 2020. Adv. Mater 32 (36), 2002171.
- Yang, J., Chen, J., Su, Y., Jing, Q., Li, Z., Yi, F., Wen, X., Wang, Z., Wang, Z.L., 2015. Adv. Mater 27 (8), 1316-1326.
- Yang, X., Zhao, Y., Xie, J., Han, X., Wang, J., Zong, C., Ji, H., Zhao, J., Jiang, S., Cao, Y., 2016. ACS Nano 10 (3), 3801-3808.
- Yi, L., Jiao, W., Wu, K., Qian, L., Yu, X., Xia, Q., Mao, K., Yuan, S., Wang, S., Jiang, Y., 2015. Nano Res. 8, 2978-2987.
- Yi, L., Jiao, W., Zhu, C., Wu, K., Zhang, C., Qian, L., Wang, S., Jiang, Y., Yuan, S., 2016. Nano Res. 9 (5), 1346-1357.
- Yin, J., Hu, P., Luo, J., Wang, L., Cohen, M.F., Zhong, C.J., 2011. ACS Nano 5 (8), 6516-6526.
- You, I., Kim, B., Park, J., Koh, K., Shin, S., Jung, S., Jeong, U., 2016. Adv. Mater 28 (30), 6359-6364.
- Yuan, L., Wang, L., Garrigues, A.R., Jiang, L., Annadata, H.V., Antonana, M.A., 2018. Nat. Nanotech 13 (4), 322-329.
- Zamborini, F.P., Bao, L.L., Dasari, R., 2012. Anal. Chem. 84 (2), 541-576.
- Zhang, M., Wang, C., Wang, H., Jian, M., Hao, X., Zhang, Y., 2017a. Adv. Funct. Mater. 27 (2), 1604795. Zhang, N., Tao, C., Fan, X., Chen, J., 2017b. J. Mater. Res. 32 (9), 1628-1646.
- Zhang, P., Bousack, H., Dai, Y., Offenhäusser, A., Mayer, D., 2018. Nanoscale 10 (3),
- Zhang, S., Bick, M., Xiao, X., Chen, G., Nashalian, A., Chen, J., 2021. Matter 4 (3),
- Zhao, W., Luo, J., Shan, S., Lombardi, J.P., Xu, Y., Cartwright, K., Lu, S., Poliks, M., Zhong, C.J., 2015a. Small 11 (35), 4509-4516.

- Zhao, W., Rovere, T., Weerawarne, D., Osterhoudt, G., Kang, N., Joseph, P., Luo, J., Shim, B., Poliks, M., Zhong, C.J., 2015b. ACS Nano 9 (6), 6168–6177. Zhou, H., Zhang, Y., Qiu, Y., Wu, H., Qin, W., Liao, Y., Yu, Q., Cheng, H., 2020a. Biosens. Bioelectron 168, 112569.
- Zhou, Z., Chen, K., Li, X., Zhang, S., Wu, Y., Zhou, Y., Meng, K., Sun, C., He, Qiang, Fan, W., Fan, E., Lin, Z., Tan, X., Deng, W., Yang, J., Chen, J., 2020b. Nat. Electron 3, 571–578.
- Zhou, Z., Padgett, S., Cai, Z., Conta, G., Wu, Y., He, Q., Zhang, S., Sun, C., Liu, J., Fan, E., Meng, K., Lin, Z., Uy, C., Yang, J., Chen, J., 2020c. Biosens. Bioelectron 155, 112064.